Dimension-free path-integral molecular dynamics without preconditioning

Roman Korol,[1] Nawaf Bou-Rabee,[2, a)] and Thomas F. Miller III[1, b)]
[1)] *Division of Chemistry and Chemical Engineering, California Institute of Technology, Pasadena, CA 91125, USA*
[2)] *Department of Mathematical Sciences Rutgers University Camden, Camden, NJ 08102 USA*

(Dated: 8 November 2019)

Convergence with respect to imaginary-time discretization (i.e., the number of ring-polymer beads) is an essential part of any path-integral-based molecular dynamics (MD) calculation. However, an unfortunate property of existing non-preconditioned numerical integration schemes for path-integral molecular dynamics (PIMD) – including essentially all existing ring-polymer molecular dynamics (RPMD) and thermostatted RPMD (T-RPMD) methods – is that for a given MD timestep, the overlap between the exact ring-polymer Boltzmann distribution and that sampled using MD becomes zero in the infinite-bead limit. This has clear implications for hybrid Metropolis Monte-Carlo/MD sampling schemes, and it also causes the well-known divergence with bead number of the primitive path-integral kinetic-energy expectation value when using standard RPMD or T-RPMD. We show that these problems can be avoided through the introduction of "dimension-free" numerical integration schemes for which the sampled ring-polymer distribution has non-zero overlap with the exact distribution in the infinite-bead limit. Moreover, we show that this can be achieved by using a (previously introduced) strongly stable method for the free-ring-polymer evolution in combination with a (newly introduced) mollification of the forces from the external physical potential. The resulting dimension-free numerical integration schemes yield finite error bounds for a given MD timestep, even as the number of beads is taken to infinity; these conclusions are proven for the case of a harmonic potential and borne out numerically for anharmonic cases. Importantly, dimension-free RPMD achieves these benefits while preserving strong stability, symplecticity, time reversibility, and global second-order accuracy; and it remains a simple, black-box method by avoiding computational costs, tunable parameters, or system-specific implementations. Numerical results illustrate that problems with the infinite-bead limit also manifest in simulations with finite bead numbers, such that dimension-free RPMD yields improved accuracy and stability in practical simulations.

I. INTRODUCTION

Considerable effort has been dedicated to the development of numerical integration schemes for imaginary-time path-integral molecular dynamics (PIMD).[1] In comparison to standard classical molecular dynamics, PIMD numerical integration faces the additional challenge of the highly oscillatory dynamics of the ring-polymer internal modes. Work on PIMD numerical integration generally falls into two distinct categories. In the first, the PIMD equations of motion are *preconditioned* by modifying the ring-polymer mass matrix;[2–10] this approach, which includes the widely used staging algorithms,[11] causes the integrated trajectories to differ from those of the ring-polymer molecular dynamics (RPMD) model for real-time dynamics,[12,13] but it can lead to efficient[4–6] sampling of the quantum Boltzmann distribution.[14,15] In the second category, no modification is made to the ring-polymer mass matrix, i.e., the equations of motion are *non-preconditioned*.[13,16–21]

With the aim of providing useful models for real-time quantum dynamics, as well as simple and efficient algorithms for equilibrium thermal sampling, the current work focuses on non-preconditioned PIMD numerical integration, notable examples of which include RPMD[12,13] and its thermostatted variant T-RPMD.[20] Numerical integration schemes for these methods typically employ symmetric factorizations of the time-evolution operator[11,16–23] such as[24]

$$e^{\Delta t\mathcal{L}} = e^{\frac{\Delta t}{2}\mathcal{L}_\gamma} e^{\frac{\Delta t}{2}\mathcal{L}_V} e^{\Delta t\mathcal{L}_0} e^{\frac{\Delta t}{2}\mathcal{L}_V} e^{\frac{\Delta t}{2}\mathcal{L}_\gamma} + \mathcal{O}(\Delta t^3) \quad (1)$$

where the operator $\mathcal{L} = \mathcal{L}_V + \mathcal{L}_0 + \mathcal{L}_\gamma$ includes contributions from the external potential, $\mathcal{L}_V$, the purely harmonic free-ring-polymer motion, $\mathcal{L}_0$, and a friction-dependent thermostat, $\mathcal{L}_\gamma$; note that the standard microcanonical RPMD numerical integration scheme is then recovered in the limit of zero coupling to the thermostat.

In our previous work,[25] we emphasized that earlier PIMD numerical integration schemes had overlooked a fundamental aspect of the $\exp(\Delta t\mathcal{L}_0)$ sub-step of the time evolution in Eq. 1. Standard practice in these integration schemes has been to exactly evolve the harmonic free ring-polymer dynamics associated with $\exp(\Delta t\mathcal{L}_0)$ using the uncoupled free ring-polymer normal modes.[11,16–18] However, this standard practice was shown to lack the

[a)] Electronic mail: nawaf.bourabee@rutgers.edu
[b)] Electronic mail: tfm@caltech.edu

property of strong stability in the numerical integration, leading to resonance instabilities for microcanonical RPMD and loss of ergodicity for T-RPMD.[25] Use of the Cayley modification to the free ring-polymer motion was shown to impart strong stability to the time-evolution, thereby improving numerical stability for microcanonical RPMD and restoring ergodicity for T-RPMD.[25]

In the current study, we emphasize that previous work has also overlooked a second, distinct problem, related to the $\exp((\Delta t/2)\mathcal{L}_V)$ sub-steps of the time evolution in Eq. 1. Naive implementation of these sub-steps can artificially cause the external force to have an outsized effect on the high-frequency internal modes. As a result, the simulated trajectories become increasingly meaningless at a fixed time step size as the number of ring-polymer beads grows. In fact, we show here that in the infinite bead limit, the stationary distribution sampled using Eq. 1 has zero overlap with the exact ring-polymer Boltzmann distribution. We also show that this artifact associated with the $\exp((\Delta t/2)\mathcal{L}_V)$ sub-steps can be easily avoided by mollifying the effect of the forces from the physical potential on the high-frequency internal ring-polymer modes.

The results presented here indicate that force mollification, when applied in combination with the recently introduced strongly stable Cayley modification for the free ring polymer evolution,[25] yields "dimension-free" integrators with both formal and practical advantages over existing non-preconditioned PIMD numerical integration schemes, including better accuracy and the ability to employ substantially larger timesteps in the calculation of both statistical and numerical properties. Importantly, these gains are made without loss of computational efficiency or algorithmic simplicity.

II. NON-PRECONDITIONED PIMD

Consider a one-dimensional molecular system with potential energy function $V(x)$ and mass m. The equations of motion for the corresponding n-bead ring polymer held at constant temperature T by a Langevin thermostat are

$$\begin{aligned}\dot{\boldsymbol{q}}(t) = \boldsymbol{v}(t)\ ,\ \dot{\boldsymbol{v}}(t) = -\boldsymbol{\Omega}^2\boldsymbol{q}(t) + \frac{1}{m_n}\boldsymbol{F}(\boldsymbol{q}(t)) \\ - \boldsymbol{\Gamma}\boldsymbol{v}(t) + \sqrt{\frac{2}{\beta m_n}}\boldsymbol{\Gamma}^{1/2}\dot{\boldsymbol{W}}(t)\ .\end{aligned} \tag{2}$$

Here, $\boldsymbol{W}$ is an n-dimensional standard Brownian motion; $\boldsymbol{q}(t) = (q_0(t), \ldots, q_{n-1}(t))$ is the vector of positions for the n ring-polymer beads at time $t \geq 0$ and $\boldsymbol{v}(t)$ are the corresponding velocities; $m_n = m/n$ and $\beta = (k_B T)^{-1}$; and $\boldsymbol{F}(\boldsymbol{q}) = -\nabla V_n^{\text{ext}}(\boldsymbol{q})$, where V_n^{ext} is the contribution of the external potential,

$$V_n^{\text{ext}}(\boldsymbol{q}) = \frac{1}{n}\sum_{j=0}^{n-1} V(q_j)\ . \tag{3}$$

Moreover, $\boldsymbol{\Omega}^2$ is the following $n \times n$ symmetric positive semi-definite matrix

$$\boldsymbol{\Omega}^2 = -\kappa_n^2 \begin{bmatrix} -2 & 1 & 0 & \cdots & 0 & 1 \\ 1 & -2 & 1 & 0 & \cdots & 0 \\ & \ddots & \ddots & \ddots & & \\ & & \ddots & \ddots & \ddots & \\ 0 & \cdots & 0 & 1 & -2 & 1 \\ 1 & 0 & \cdots & 0 & 1 & -2 \end{bmatrix}, \tag{4}$$

where $\kappa_n = n/(\hbar\beta)$. Note that $\boldsymbol{\Omega}$ can be diagonalized by an $n \times n$ orthonormal real discrete Fourier transform matrix $\boldsymbol{U}$ as follows

$$\boldsymbol{\Omega} = \boldsymbol{U}\,\mathrm{diag}(0, \omega_{1,n}, \ldots, \omega_{n-1,n})\boldsymbol{U}^{\mathrm{T}}, \tag{5}$$

where $\omega_{j,n}$ is the jth Matsubara frequency[26] given by

$$\omega_{j,n} = \begin{cases} 2\kappa_n \sin\left(\frac{\pi j}{2n}\right) & \text{if } j \text{ is even}\ , \\ 2\kappa_n \sin\left(\frac{\pi(j+1)}{2n}\right) & \text{else}\ . \end{cases} \tag{6}$$

Finally, the matrix $\boldsymbol{\Gamma}$ in Eq. 2 is typically an $n \times n$ symmetric positive semi-definite friction matrix of the form

$$\boldsymbol{\Gamma} = \boldsymbol{U}\,\mathrm{diag}(0, \gamma_1, \ldots, \gamma_{n-1})\boldsymbol{U}^{\mathrm{T}}, \tag{7}$$

where γ_j is the friction factor in the jth normal mode.

In RPMD and T-RPMD calculations, one is often interested in the dynamics of Eq. 2 with initial conditions drawn from the stationary distribution with non-normalized density $\exp(-\beta H_n(\boldsymbol{q}, \boldsymbol{v}))$, where $H_n(\boldsymbol{q}, \boldsymbol{v})$ is the ring polymer Hamiltonian defined by

$$H_n(\boldsymbol{q}, \boldsymbol{v}) = H_n^0(\boldsymbol{q}, \boldsymbol{v}) + V_n^{\text{ext}}(\boldsymbol{q}), \tag{8}$$

and $H_n^0(\boldsymbol{q}, \boldsymbol{v}) = (1/2)m_n\left(|\boldsymbol{v}|^2 + \boldsymbol{q}^{\mathrm{T}}\boldsymbol{\Omega}^2\boldsymbol{q}\right)$ is the free ring-polymer Hamiltonian.

The standard method for implementing the splitting in Eq. 1 consists of five sub-steps: (i) an Ornstein-Uhlenbeck half timestep

$$\boldsymbol{v} \leftarrow \exp(-(\Delta t/2)\boldsymbol{\Gamma})\boldsymbol{v} + \sqrt{\frac{1}{\beta m_n}}(\boldsymbol{I} - \exp(-\Delta t\boldsymbol{\Gamma}))^{1/2}\boldsymbol{\xi} \tag{9}$$

where $\boldsymbol{I}$ is the $n \times n$ identity matrix and $\boldsymbol{\xi} \sim \mathcal{N}(0,1)^n$; (ii) a half timestep from the forces of the external potential

$$\boldsymbol{v} \leftarrow \boldsymbol{v} + \frac{\Delta t}{2}\frac{1}{m_n}\boldsymbol{F}(\boldsymbol{q}) \tag{10}$$

(iii) a full timestep of the exact free ring-polymer dynamics

$$\begin{pmatrix}\boldsymbol{q} \\ \boldsymbol{v}\end{pmatrix} \leftarrow \exp(\Delta t\boldsymbol{\mathcal{A}})\begin{pmatrix}\boldsymbol{q} \\ \boldsymbol{v}\end{pmatrix}, \tag{11}$$

where $\boldsymbol{\mathcal{A}} = \begin{bmatrix}\boldsymbol{0} & \boldsymbol{I} \\ -\boldsymbol{\Omega}^2 & \boldsymbol{0}\end{bmatrix}$ is the Hamiltonian matrix associated to the free ring polymer; (iv) another half timestep

of Eq. 10; and finally, (v) another half timestep of Eq. 9. As is common, we shall refer to this integration scheme as "OBABO", where each letter in the acronym indicates one of the five sequential sub-steps.

In recent work,[25] we showed that the matrix exponential for the free ring-polymer evolution in Eq. 11 is not a strongly stable symplectic matrix, and as a consequence, OBABO can become non-ergodic at timesteps $\Delta t = k\pi/\omega_{j,n}$ for any $1 \leq j \leq n$ and $k \geq 1$. We also identified a maximum safe timestep size $\Delta t_\star = \beta\hbar\pi/(2n)$, below which the matrix exponential is strongly stable. Unfortunately, as $n \to \infty$, this maximum safe timestep goes to zero, such that no finite timestep for the OBABO scheme is safe in this limit from non-ergodicity.

This non-ergodicity of OBABO motivated the Cayley modification[25] which consists of approximating the matrix exponential in Eq. 11 with the Cayley transform

$$\mathrm{cay}(\Delta t\boldsymbol{\mathcal{A}}) = (\boldsymbol{I} - (1/2)\Delta t\boldsymbol{\mathcal{A}})^{-1}(\boldsymbol{I} + (1/2)\Delta t\boldsymbol{\mathcal{A}}) \ . \quad (12)$$

The resulting integration scheme is termed "OBCBO." The Cayley transform is strongly stable, and hence, the OBCBO integration scheme remains ergodic for a fixed timestep, irrespective of the number of beads. Moreover, like OBABO, OBCBO exhibits locally third-order accuracy in the timestep and leaves invariant the free ring-polymer Boltzmann-Gibbs distribution in the special case of a constant external potential ($V \equiv$ const.).[25]

III. PATHOLOGIES IN THE INFINITE BEAD LIMIT

The "B" sub-step of the OBABO and OBCBO integration schemes (Eq. 10) incorporates the effect of the external potential on the simulated trajectories. As will be shown, updating the velocities in this way has an outsized effect in the high-frequency ring-polymer internal modes, where the exact dynamics should be dominated by the harmonic motion of the free ring polymer. As a consequence, use of the "B" sub-step in the OBABO and OBCBO schemes leads to zero overlap between the numerically sampled stationary distribution and the exact stationary distribution in the limit of large bead numbers. Here, we prove that this pathology emerges in the specific context of a harmonic external potential for non-preconditioned integrators that make direct use of Eq. 10, and as expected, numerical evidence given in Section VII indicates that the problem also

manifests for anharmonic potentials. .

To this end, consider the j^{th} internal ring-polymer mode with frequency $\omega_{j,n}$, in the presence of a harmonic external potential $V(q) = (1/2)\Lambda q^2$ and a Langevin thermostat with friction γ_j. Expressed in terms of the normal mode coordinates, obtained from the Cartesian positions and velocities via the orthogonal transformation

$$\boldsymbol{\varrho} = \boldsymbol{U}^{\mathrm{T}}\boldsymbol{q} \qquad \text{and} \qquad \boldsymbol{\varphi} = \boldsymbol{U}^{\mathrm{T}}\boldsymbol{v} \quad (13)$$

where $\boldsymbol{U}$ is defined in Eq. 5, the non-preconditioned PIMD equations of motion for this mode are

$$\begin{bmatrix}\dot{\varrho}_j(t)\\ \dot{\varphi}_j(t)\end{bmatrix} = \boldsymbol{K}_j\begin{bmatrix}\varrho_j(t)\\ \varphi_j(t)\end{bmatrix} + \begin{bmatrix}0\\ \sqrt{2\beta^{-1}m_n^{-1}\gamma_j}\dot{W}_j(t)\end{bmatrix} \quad (14)$$
$$\boldsymbol{K}_j = \boldsymbol{\mathcal{A}}_j + \boldsymbol{\mathcal{B}} + \boldsymbol{\mathcal{C}}_j,$$

where $\dot{W}_j$ is a scalar white-noise, and we have introduced the following 2×2 matrices

$$\boldsymbol{\mathcal{A}}_j = \begin{bmatrix}0 & 1\\ -\omega_{j,n}^2 & 0\end{bmatrix}, \ \boldsymbol{\mathcal{B}} = \begin{bmatrix}0 & 0\\ -\Lambda/m & 0\end{bmatrix}, \text{ and } \boldsymbol{\mathcal{C}}_j = \begin{bmatrix}0 & 0\\ 0 & -\gamma_j\end{bmatrix}.$$

The solution $(\varrho_j(t), \varphi_j(t))$ of Eq. 14 is a bivariate Gaussian, and in the limit as $t \to \infty$, the probability distribution of $(\varrho_j(t), \varphi_j(t))$ converges to a centered bivariate normal distribution with covariance matrix

$$\boldsymbol{\Sigma}_j = \frac{1}{\beta m_n}\begin{bmatrix}s_j^2 & 0\\ 0 & 1\end{bmatrix}, \qquad s_j^2 = \frac{1}{\Lambda/m + \omega_{j,n}^2}. \quad (15)$$

For this system, a single timestep of OBABO yields

$$\begin{bmatrix}\varrho_j(t+\Delta t)\\ \varphi_j(t+\Delta t)\end{bmatrix} = \boldsymbol{O}_j\boldsymbol{M}_j\boldsymbol{O}_j\begin{bmatrix}\varrho_j(t)\\ \varphi_j(t)\end{bmatrix} + \boldsymbol{R}_j^{1/2}\begin{bmatrix}\xi_0\\ \eta_0\end{bmatrix}, \quad (16)$$

where ξ_0, η_0 are independent standard normal random variables, and we have introduced the following 2×2 matrices

$$\boldsymbol{M}_j = e^{\frac{\Delta t}{2}\boldsymbol{\mathcal{B}}}\exp(\Delta t\boldsymbol{\mathcal{A}}_j)e^{\frac{\Delta t}{2}\boldsymbol{\mathcal{B}}}, \quad \boldsymbol{O}_j = e^{\frac{\Delta t}{2}\boldsymbol{\mathcal{C}}_j},$$
$$\boldsymbol{R}_j = \frac{1-e^{-\gamma_j\Delta t}}{\beta m_n}\left(\boldsymbol{O}_j\boldsymbol{M}_j\begin{bmatrix}0 & 0\\ 0 & 1\end{bmatrix}(\boldsymbol{O}_j\boldsymbol{M}_j)^{\mathrm{T}} + \begin{bmatrix}0 & 0\\ 0 & 1\end{bmatrix}\right).$$

The corresponding step for OBCBO is obtained by replacing $\exp(\Delta t\boldsymbol{\mathcal{A}}_j)$ in $\boldsymbol{M}_j$ with $\mathrm{cay}(\Delta t\boldsymbol{\mathcal{A}}_j)$. A sufficient condition[27] for ergodicity in the j^{th} internal ring-polymer mode is

$$1 > \mathsf{A}_{j,\Delta t}^2\cosh^2((\Delta t/2)\gamma_j), \quad \text{where}$$
$$\mathsf{A}_{j,\Delta t} = \begin{cases}\cos_j - \dfrac{(\Lambda/m)\Delta t}{2\omega_{j,n}}\sin_j & \text{for OBABO}\ , \\ -1 + \dfrac{8 - 2(\Lambda/m)\Delta t^2}{4 + \omega_{j,n}^2\Delta t^2} & \text{for OBCBO}\ . \end{cases} \quad (17)$$

Here, we used the shorthand notation $\cos_j = \cos(\Delta t\omega_{j,n})$ and $\sin_j = \sin(\Delta t\omega_{j,n})$. Due to a lack of strong stability in the "A" sub-step, OBABO fails to meet this condition and becomes non-ergodic whenever $\Delta t = k\pi/\omega_{j,n}$ where $k \geq 1$;[25] no such problem exists for OBCBO. Regardless, assuming that the condition in Eq. 17 holds, the numerical stationary distribution is a centered Gaussian with 2×2 covariance matrix $\boldsymbol{\Sigma}_{j,\Delta t}$ that satisfies the linear equation

$$\boldsymbol{\Sigma}_{j,\Delta t} = \boldsymbol{O}_j\boldsymbol{M}_j\boldsymbol{O}_j\boldsymbol{\Sigma}_{j,\Delta t}(\boldsymbol{O}_j\boldsymbol{M}_j\boldsymbol{O}_j)^{\mathrm{T}} + \boldsymbol{R}_j\ ,$$

for which the solution is

$$\mathbf{\Sigma}_{j,\Delta t} = \frac{1}{\beta m_n}\begin{bmatrix} s^2_{j,\Delta t} & 0 \\ 0 & 1 \end{bmatrix} \tag{18}$$

where the variance in the position-marginal is $(\beta m_n)^{-1} s^2_{j,\Delta t}$ with

$$s^2_{j,\Delta t} = \begin{cases} \dfrac{1}{\omega^2_{j,n} + \frac{\Lambda \Delta t \omega_{j,n}}{m}\cot_j - (\frac{\Lambda \Delta t}{2m})^2} & \text{for OBABO} \\ \dfrac{4m}{4m - \Delta t^2 \Lambda} s^2_j & \text{for OBCBO} \end{cases} \tag{19}$$

and where $\cot_j = \cot(\Delta t \omega_{j,n})$. Note that this numerical stationary distribution does not involve the friction parameter γ_j, which is a key benefit of using the exact Ornstein-Uhlenbeck flow in Eq. 9. Moreover, comparing the exact covariance matrix in Eq. 15 with the approximations in Eqs. 18 and 19, note that $\mathbf{\Sigma}_j = \lim_{\Delta t \to 0} \mathbf{\Sigma}_{j,\Delta t}$, and that the variance of the velocity-marginal is exact while there is finite-timestep error in the variance of the position-marginal.[8,28]

In normal mode coordinates, the exact and numerical position-marginals can be written as an infinite product of one-dimensional centered normal distributions with variances given by $(\beta m_n)^{-1} s^2_j$ and $(\beta m_n)^{-1} s^2_{j,\Delta t}$, respectively. By Kakutani's theorem,[29,30] these two distributions have a nonzero overlap in the infinite bead limit if and only if the following series converges,

$$\sum_{j=1}^{\infty} \left(1 - \frac{s_j}{s_{j,\Delta t}}\right)^2 . \tag{20}$$

For OBABO, due to the oscillatory cotangent term appearing in $s_{j,\Delta t}$, the limit $\lim_{j\to\infty}(1 - s_j/s_{j,\Delta t})^2$ does not exist, and therefore, the series does not converge. For OBCBO, the jth summand of this series is

$$\frac{\Delta t^4 \Lambda^2}{16 m^2}\left(1 + \sqrt{\frac{4m - \Delta t^2 \Lambda}{4m}}\right)^{-2} ,$$

which more obviously diverges. Therefore, for both OBABO and OBCBO, the numerical stationary distribution has no overlap with the exact stationary distribution in the infinite bead limit.

We emphasize again that in the absence of a physical potential, both the OBABO and OBCBO schemes leave invariant the exact free ring-polymer Boltzmann-Gibbs distribution.[25] Therefore, the loss of any overlap between the exact stationary distribution in the infinite bead limit for the OBABO or OBCBO numerical integration schemes described in this section must be attributed to the influence of the time-evolution from the external potential in the schemes (i.e., the "B" sub-step) as implemented in Eq. 10.

IV. CONSEQUENCES FOR THE PRIMITIVE KINETIC ENERGY EXPECTATION VALUE

In the current section, we show that the non-overlap pathology of the OBABO and OBCBO schemes causes a divergence with increasing bead number of the primitive path-integral kinetic-energy expectation value, an issue that is numerically well known[8,28,31,32] but which has not been fully understood mathematically.

The primitive kinetic energy expectation value is given by[33,34]

$$\langle KE \rangle = \frac{n}{2\beta} - \sum_{j=1}^{n} \frac{m_n \kappa_n^2}{2} \langle (q_j - q_{j-1})^2 \rangle \tag{21}$$

$$= \frac{1}{2\beta} + \sum_{j=1}^{n-1} \left(\frac{1}{2\beta} - \frac{m_n \omega^2_{j,n}}{2} \langle \varrho_j^2 \rangle \right) \tag{22}$$

where the first equality involves a sum over the ring-polymer beads in Cartesian coordinates (with $q_n = q_0$), and the second equality performs the summation in terms of the ring-polymer normal modes. The divergence of this expectation value is numerically illustrated for the simple case of a harmonic oscillator (Fig. 1a-d); note that for larger MD timesteps, the OBABO and OBCBO schemes fail to reach a plateau with increasing bead number and dramatically deviate from the exact result (black dashed line). The same divergence has been numerically observed in many systems, including liquid water, for simulations employing OBABO (and related integration schemes composed of these sub-steps).[8,28,31,32]

Using Eq. 15, note that the contribution to the primitive kinetic energy expectation value from the jth ring-polymer mode is

$$\langle KE_j \rangle = \frac{1}{2\beta}\left(1 - \omega^2_{j,n} s^2_j\right) ,$$

such that in the infinite bead limit,

$$\lim_{n\to\infty} \sum_{j=0}^{n-1} \langle KE_j \rangle = \frac{\hbar}{4}\sqrt{\frac{\Lambda}{m}}\left(1 + \frac{2}{e^{\hbar\beta\sqrt{\Lambda/m}} - 1}\right) . \tag{23}$$

Using Eqs. 18 and 19, the jth-mode contribution to the kinetic energy from the finite-timestep numerical expectation value is

$$\langle KE_j \rangle_{\Delta t} = \frac{1}{2\beta}\left(1 - \omega^2_{j,n} s^2_{j,\Delta t}\right) . \tag{24}$$

Thus, the per-mode error is

$$|\langle KE_j \rangle - \langle KE_j \rangle_{\Delta t}| = \frac{1}{2\beta}\omega^2_{j,n} s^2_j \left|1 - \frac{s^2_{j,\Delta t}}{s^2_j}\right| , \tag{25}$$

where $s_{j,\Delta t}$ for the separate cases of OBABO and OBCBO is given in Eq. 19. Since $\omega^2_{j,n} s^2_j \to 1$ as

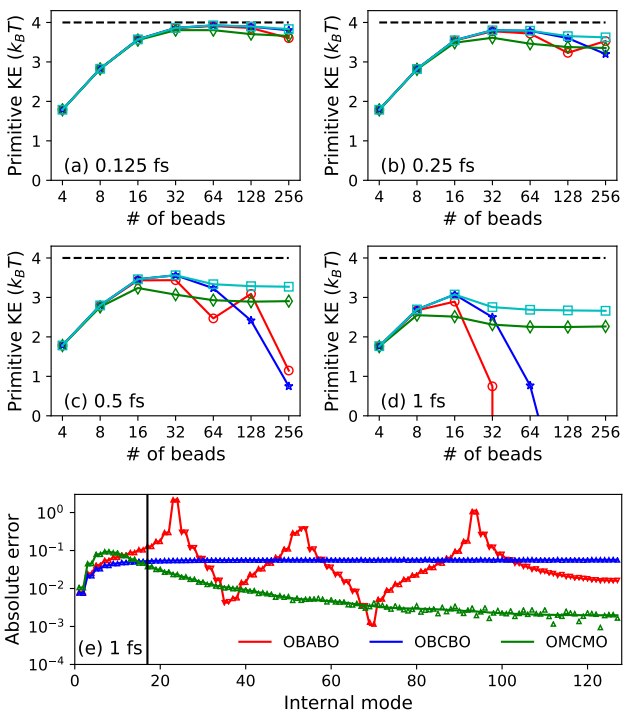

FIG. 1. **Primitive kinetic energy expectation values** for a harmonic potential $V(q) = \frac{1}{2}\Lambda q^2$ with $\Lambda = 256$, $\hbar = m = 1$, and reciprocal temperature $\beta = 1$; choosing energies to be in units of $k_\mathrm{B}T$ at room temperature (300 K), then $\beta\hbar \approx 25.5$ fs and $\Lambda = \sqrt{m\omega^2}$ where $\omega = 3315$ cm^{-1}. (a-d) For various MD timesteps, the primitive kinetic energy expectation value as a function of the number of ring-polymer beads, with the exact kinetic energy indicated as a dashed line. (e) Per-mode error in the primitive kinetic energy expectation value for simulations run with 128 ring-polymer beads and a timestep of 1 fs; solid lines are analytic predictions from Eq. 25, and points indicate the results of numerical PIMD simulations using the various integration schemes. The black vertical line indicates the crossover frequency ($\omega_\mathrm{x} = 2/\Delta t$) for the error of OBCBO and OBMBO based on the bounds in Eqs. 35 and 36.

$n \to \infty$, the convergence of $\sum_{j=1}^{\infty} |\langle KE_j\rangle - \langle KE_j\rangle_{\Delta t}|$ basically reduces to the convergence of the series $\sum_{j=1}^{\infty} \left|1 - s_{j,\Delta t}^2/s_j^2\right|$, which diverges for both OBABO and OBCBO due to the same reasons as discussed in the previous section. Note that the right-hand-side of equation of Eq. 25 involes the error in the variance of the j^{th} ring-polymer internal mode, $\left|s_j^2 - s_{j,\Delta t}^2\right|$, a fundamental measure of the error of the numerically sampled ring-polymer stationary distribution.

For the case of a harmonic external potential, Fig. 1e shows the per-mode error for the primitive kinetic energy expectation value of the OBABO (red) and OBCBO (blue) schemes using a timestep of 1 fs, with the solid lines indicating the analytical predictions in Eq. 25 and with the dots indicating the result of numerical simulations. The analytical results are fully reproduced by the simulations. Note that the OBABO per-mode error exhibits dramatic spikes for $\omega_{j,n}\Delta t = k\pi$ where $1 \le j \le n$ and for some $k \ge 1$, which coincide with the loss of ergodicity of that integration scheme. However, it is the failure of this per-mode error to decay as a function of the mode number for both OBABO and OBCBO that gives rise upon summation to the divergence of the primitive kinetic energy expectation value, as seen for this particular timestep in Fig. 1d.

V. DIMENSIONALITY FREEDOM VIA FORCE MOLLIFICATION

To improve the strongly stable OBCBO integration scheme, we now show that the pathology with the "B" sub-step can be removed, and overlap with the exact stationary distribution restored. This is achieved with a general force-mollification strategy, in which the external potential energy in Eq. 3 is replaced by

$$\tilde{V}_n^{\text{ext}}(\boldsymbol{q}) = V_n^{\text{ext}}(\mathrm{sinc}(\tilde{\boldsymbol{\Omega}}\Delta t/2)\boldsymbol{q}), \tag{26}$$

where $\tilde{\boldsymbol{\Omega}}$ is any positive semi-definite $n \times n$ matrix that has the same eigenvectors as $\boldsymbol{\Omega}$ (Eq. 5) while possibly having different eigenvalues. Force mollification has not previously been employed for PIMD, although the strategy originates from a variation-of-constants formulation of the solution to Eq. 2;[35–38] specifically, the protocol in Eq. 26 is a generalization of the mollified impulse method.[35]

Use of force mollification in the current work can also be motivated on physical grounds: We have previously emphasized that the pathologies of OBABO and OBCBO with regard to mode convergence arise from the outsized effect of the external forces on the high-frequency ring-polymer internal modes when using the "B" sub-step. We thus use mollification to reduce the external forces on the high-frequency modes, such that the resulting integration correctly reverts to free-particle motion for those modes, which should become decoupled from the external potential as the frequency increases. The specific appearance of the 1/2 factor in the sinc function argument ensures that the sinc function switches from its high-frequency effect to its low-frequency effect when the period of the Matsubara frequency is commensurate with Δt; the zero-frequency ring-polymer centroid mode is untouched by mollification.

Force mollification requires only a small algorithmic modification of standard integrators. Specifically, the "B" sub-step in Eq. 10 is replaced with

$$\boldsymbol{v} \leftarrow \boldsymbol{v} + \frac{\Delta t}{2}\frac{1}{m_n}\tilde{\boldsymbol{F}}(\boldsymbol{q}), \tag{27}$$

where the mollified forces are

$$\tilde{\boldsymbol{F}}(\boldsymbol{q}) = \mathrm{sinc}(\tilde{\boldsymbol{\Omega}}\Delta t/2)\boldsymbol{F}(\tilde{\boldsymbol{q}}) = \boldsymbol{U}\boldsymbol{D}_{\Delta t}\boldsymbol{U}^{\mathrm{T}}\boldsymbol{F}(\tilde{\boldsymbol{q}}) \tag{28}$$

where $\tilde{\boldsymbol{q}} = \boldsymbol{U}\boldsymbol{D}_{\Delta t}\boldsymbol{U}^{\mathrm{T}}\boldsymbol{q}$ are the mollified bead positions, and where $\boldsymbol{D}_{\Delta t}$ is the diagonal matrix of eigenvalues associated with $\mathrm{sinc}(\tilde{\boldsymbol{\Omega}}\Delta t/2)$, i.e.,

$$\boldsymbol{D}_{\Delta t} = \mathrm{diag}(\mathrm{sinc}(\tilde{\omega}_{0,n}\Delta t/2), \ldots, \mathrm{sinc}(\tilde{\omega}_{n-1,n}\Delta t/2)) \tag{29}$$

where $\tilde{\omega}_{j,n}$ is the jth eigenvalue of $\tilde{\boldsymbol{\Omega}}$. In practice, the mollified forces are computed in normal mode coordinates as follows:

(a) Starting with the ring-polymer bead position in normal mode coordinates, obtain a copy of the mollified bead positions via

$$\tilde{\boldsymbol{q}} = \boldsymbol{U}\boldsymbol{D}_{\Delta t}\boldsymbol{\varrho}\,. \tag{30}$$

(b) Evaluate the external forces at the mollified ring-polymer bead positions, $\boldsymbol{F}(\tilde{\boldsymbol{q}})$.

(c) Apply the remaining mollification to the forces in Eq. 28 via

$$\boldsymbol{U}^{\mathrm{T}}\tilde{\boldsymbol{F}}(\boldsymbol{q}) = \boldsymbol{D}_{\Delta t}\boldsymbol{U}^{\mathrm{T}}\boldsymbol{F}(\tilde{\boldsymbol{q}})\,. \tag{31}$$

We emphasize that in comparison to the standard force update (Eq. 10) the use of the mollified force update (Eq. 27) introduces neither additional evaluations of the external forces nor $n \times n$ matrix multiplies associated with the discrete Fourier transform; it therefore avoids any significant additional computational cost.

This mollification scheme preserves reversibility and symplecticity as well as local-third order accuracy of the OBCBO scheme with timestep. We emphasize that the sinc-function-based mollification scheme in Eq. 27 is not unique, and alternatives can certainly be devised. Even within the functional form of the mollification in Eq. 27, flexibility remains with regard to the choice of the matrix $\tilde{\boldsymbol{\Omega}}$, which allows for mode-specificity in the way the mollification is applied. A simple choice for this matrix is $\tilde{\boldsymbol{\Omega}} = \boldsymbol{\Omega}$, such that mollification is applied to all of the non-zero ring-polymer internal modes. With this choice, we arrive at a fully-specified integration scheme that replaces the original "B" sub-step in Eq. 10 with the mollified-force sub-step in Eq. 27; we shall refer to this non-preconditioned PIMD numerical integration scheme as "OMCMO." In the following section, we propose an alternative choice for $\tilde{\boldsymbol{\Omega}}$ that further improves accuracy.

For the harmonic external potential, all of the previously derived relations for OBCBO (most notably Eqs. 17, 19, and 25) also hold for OMCMO with Λ suitably replaced by $\tilde{\Lambda}_j = \mathrm{sinc}^2(\omega_{j,n}\Delta t/2)\Lambda$. Note that $\tilde{\Lambda}_j \leq \Lambda$, since $\mathrm{sinc}^2(\mathsf{x}) \leq 1$ for all $\mathsf{x} \geq 0$, making clear that the mollification reduces the effect of the external potential on the higher-frequency internal ring-polymer modes.

We now show that mollifying the forces in the B sub-step fixes the pathologies of OBCBO and OBABO in the infinite-bead limit, by restoring overlap between the sampled and exact stationary distributions. To see this, note that the jth summand in Eq. 20 for OMCMO satisfies

$$\left(1 - \frac{s_j}{s_{j,\Delta t}}\right)^2 \leq \left(1 - \frac{s_j^2}{s_{j,\Delta t}^2}\right)^2 \leq f(\omega_j\Delta t/2)\frac{\Delta t^4\Lambda^2}{16m^2}$$

where $f(\mathsf{x}) = ((1-\mathrm{sinc}^2(\mathsf{x}))/\mathsf{x}^2 + \mathrm{sinc}^2(\mathsf{x}))^2$, and we have used the infinite-bead limit for the ring-polymer internal-mode frequencies

$$\omega_j = \lim_{n\to\infty}\omega_{j,n} = \begin{cases} \dfrac{\pi j}{\hbar\beta} & \text{if } j \text{ is even}\,, \\ \dfrac{\pi(j+1)}{\hbar\beta} & \text{else}\,. \end{cases} \tag{32}$$

Since

$$\sum_{j=1}^{\infty} f(\omega_j\Delta t/2) \leq 6\frac{\hbar\beta}{\pi\Delta t} + 4\,,$$ [39]

we obtain

$$\sum_{j=1}^{\infty}\left(1 - \frac{s_j}{s_{j,\Delta t}}\right)^2 \leq \left(6\frac{\hbar\beta}{\pi\Delta t} + 4\right)\frac{\Delta t^4\Lambda^2}{16m^2}\,. \tag{33}$$

Again invoking Kakutani's theorem (Eq. 20), it follows that the numerical stationary distribution has an overlap with the exact stationary distribution. As a byproduct of this analysis, we can also quantify the amount of overlap between the exact and numerically sampled stationary distributions,[40] revealing that the total variation distance[41] between these distributions is given by

$$d_{\mathrm{TV}}(\mu, \mu_{\Delta t}) \leq \sqrt{\left(6\frac{\hbar\beta}{\pi\Delta t} + 4\right)}\frac{\Delta t^2\Lambda}{2m}\,. \tag{34}$$

In summary, the force mollification strategy introduced here provably removes the pathologies due to the "B" sub-step in the case of a harmonic oscillator potential. Moreover, for any finite number of beads, the total variation distance between the exact and numerically sampled stationary distribution can be bounded by Eq. 34, and thus, OMCMO admits error bounds that are dimension-free.

Before proceeding, we first return to Fig. 1 to compare the accuracy of OMCMO with the un-mollified OBABO and OBCBO schemes for the primitive kinetic-energy expectation value for the harmonic oscillator. As seen in panel e for the results with a timestep of 1 fs, only the per-mode error obtained by the mollified scheme (OMCMO, green) decays with mode number. Panel d then shows that upon summation of the per-mode contributions, the OMCMO prediction for the primitive kinetic energy nicely converges with respect to the number of ring-polymer beads, whereas OBABO and OBCBO

fail as discussed earlier. Similar behavior is seen for shorter MD timesteps (panels a-c), although the failure of OBCBO and OBABO becomes less severe with this range of bead-numbers as the timestep is reduced.

Although it is satisfying that mollification via OMCMO both formally and numerically fixes the problems of the non-preconditioned PIMD in the high-bead-number limit, the OMCMO results in Fig. 1 are not ideal, since in some cases the OMCMO error is substantially larger than that of OBABO or OBCBO when a modest number of beads is used (e.g., for 16 beads in panel d). This observation points to a simple and general refinement of the OMCMO scheme, which we discuss in the following section.

VI. PARTIAL MOLLIFICATION

Comparison of the per-mode errors from OBCBO and OMCMO in Fig. 1e reveals that lower errors for OMCMO are only enjoyed for internal modes that exceed a particular frequency (indicated by the vertical black line). This observation suggests that if a "crossover frequency" could be appropriately defined, then a refinement to OMCMO could be introduced for which mollification is applied only to the ring-polymer internal modes with frequency that exceed this crossover value.

For the case of a harmonic external potential, this crossover frequency ω_{x} can be found by comparing a bound for the per-mode error (Eq. 25) for OBCBO

$$|\langle KE_j\rangle - \langle KE_j\rangle_{\Delta t}| \leq \left(\frac{1}{2\beta}\frac{\Delta t^2\Lambda}{4m-\Delta t^2\Lambda}\right) \tag{35}$$

to that for OMCMO

$$|\langle KE_j\rangle - \langle KE_j\rangle_{\Delta t}| \leq g(\omega_{j,n}\Delta t/2)\left(\frac{1}{2\beta}\frac{\Delta t^2\Lambda}{4m-\Delta t^2\Lambda}\right), \tag{36}$$

where $g(\mathsf{x}) = (1-\mathrm{sinc}^2(\mathsf{x}))/\mathsf{x}^2 + \mathrm{sinc}^2(\mathsf{x})$. Since $g(\mathsf{x}) \geq 1$ only when $\mathsf{x} \leq 1$, we expect better accuracy if mollification is only applied to those ring-polymer internal modes with frequencies $\omega_{j,n} \geq \omega_{\mathrm{x}}$, where $\omega_{\mathrm{x}} = 2/\Delta t$. Remarkably, although this result was derived for the case of a harmonic potential, it does not depend on Λ. We call this resulting partly mollified integration scheme "OmCmO." This scheme preserves all of the appealing features of OMCMO, including strong stability and dimensionality freedom.

Implementation of OmCmO is a trivial modification of OMCMO, requiring only that the diagonal elements of $\boldsymbol{D}_{\Delta t}$ in Eq. 29 are evaluated using

$$\mathrm{sinc}(\tilde{\omega}_{j,n}\Delta t/2) = \begin{cases} 1 & \text{for } \omega_{j,n} < \omega_{\mathrm{x}} \\ \mathrm{sinc}(\omega_{j,n}\Delta t/2) & \text{otherwise,} \end{cases} \tag{37}$$

where $j = 0, \ldots, n-1$. In physical terms, the emergence of $2/\Delta t$ in the crossover frequency is intuitive, since as was previously mentioned, it corresponds to having the ring-polymer mode undergo a full period per timestep Δt.

Finally, numerical results for the case of a harmonic potential (Figs. 1a-d) reveal that the partially modified OmCmO scheme (cyan) achieves both robust convergence of the primitive kinetic energy with increasing bead number, as well as consistently better accuracy than any of these other non-preconditioned PIMD integration schemes – as expected.

VII. RESULTS FOR ANHARMONIC POTENTIALS

Having numerically characterized the performance of the various non-preconditioned PIMD integrators for the case of the harmonic oscillator external potential in Fig. 1, we now turn our attention to anharmonic external potentials. In this section, we consider both a weakly anharmonic (aHO) potential

$$V(q) = \Lambda\left(\frac{1}{2}q^2 + \frac{1}{10}q^3 + \frac{1}{100}q^4\right) \tag{38}$$

and the more strongly anharmonic quartic potential

$$V(q) = \frac{1}{4}q^4. \tag{39}$$

All calculations are performed using $\hbar = 1$, $m = 1$, and $\beta = 1$. For the aHO potential, we present results using both $\Lambda = 256$ and 1. Assuming the energies to be in units of $k_{\mathrm{B}}T$ at room temperature (300 K), then the thermal timescale corresponds to $\beta\hbar \approx 25.5$ fs and $\Lambda = \sqrt{m\omega^2}$ where $\omega = 3315$ cm^{-1} and 207 cm^{-1} for $\Lambda = 256$ and 1, respectively. The trajectories are performed with the centroid mode uncoupled from the thermostat (i.e., in the manner of T-RPMD); for the remaining $n-1$ internal modes, simulations performed with the OBABO scheme use the standard[18,20] damping schedule of $\boldsymbol{\Gamma} = \boldsymbol{\Omega}$, and simulations performed using the Cayley modification (i.e., OBCBO, OMCMO, and OmCmO) use friction $\gamma_j = \min(\omega_{j,n}, 0.9\gamma_j^{\max}(\Lambda), 0.9\gamma_j^{\max}(0))$ for the j^{th} mode, where $\gamma_j^{\max}(\Lambda)$ is the friction that saturates the inequality in Eq. 17; for the quartic potential, we set $\Lambda = 1$ in this calculation of $\gamma_j^{\max}$.

Figure 2 presents kinetic energy expectation values for the aHO potential corresponding to 3315 cm^{-1} at room temperature. For the primitive kinetic energy expectation value, the results obtained using the various integration schemes with timesteps of both 0.5 fs (panel a) and 1.0 fs (panel b) are consistent with the observations for the harmonic potential in Fig. 1; specifically, the unmollified integrators (OBABO and OBCBO) fail to converge with increasing bead number, while the mollified

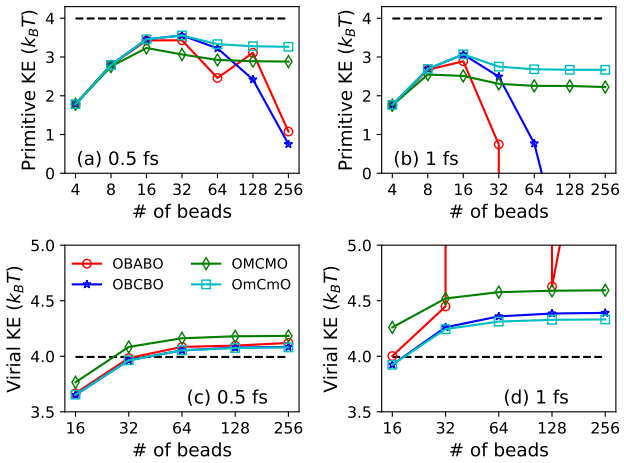

FIG. 2. **Primitive and virial kinetic energy expectation values** as a function of bead number for the weakly anharmonic potential corresponding to 3315 cm^{-1} at room temperature, with results obtained using a timestep of 0.5 fs (a,c) and 1.0 fs (b,d). The exact kinetic energy is indicated with a dashed line.

integrators (OMCMO and OmCmO) smoothly converge with increasing bead number, and the partially mollified scheme (OmCmO) is consistently more accurate than the other integration schemes. Panels c and d present the corresponding results for the virial kinetic energy expectation value. Whereas the virial kinetic energy for all of the strongly stable integration schemes is well behaved, the OBABO scheme performs erratically at the larger timesteps due to its provable non-ergodicities.[25] Appealingly, the partially mollified scheme (OmCmO) is consistently the most accurate for the virial kinetic energy expectation value, as it was for the primitive kinetic energy expectation value.

Figure 3 shows the results of the various numerical integration schemes for the primitive and virial kinetic energy expectation values, as a function of the MD timestep using 64 ring-polymer beads. Results are shown for the aHO with both high (panels a,b) and low frequency (c,d), which are chosen to resemble the characteristic vibrational frequencies of liquid water. Also included are results for the strongly anharmonic quartic oscillator. Whereas the accuracy of all of the integration schemes decays with larger MD timestep, as must be the case, it is seen that the partially mollified OmCmO scheme is consistently the most accurate across this array of model systems. Note that the range of timesteps for the lower-frequency anharmonic oscillator and quartic oscillator extend to surprisingly large timestep sizes, with the mollified schemes remaining reasonably accurate.

Taken together, the numerical results of Figs. 2 and 3a-f indicate that the advantages of the dimension-free mollified integration schemes that were rigorously proven for the case of the harmonic external potential may also extend in practice to anharmonic potential energy surfaces. Finally, Fig. 3g illustrates the use of the OmCmO integrator for the calculation of real-time quantum dynamics, which we call dimension-free (DF) RPMD. DF-RPMD involves integrating trajectories using the OmCmO scheme and interpreting those trajectories in terms of the usual RPMD model for real-time dynamics;[13] it is distinct from the T-RPMD method[20], which employs the OBABO scheme and inherits the shortcomings of the A and B sub-steps of that integrator. Using 64 beads, the DF-RPMD results are plotted for a range of integration timesteps. It is confirmed that the small-timestep DF-RPMD results are graphically indistinguishable those of small-timestep T-RPMD; the two methods become identical in the small-timestep limit for a given number of beads. However, even when DF-RPMD is employed with a timestep of 8 fs, beyond the range of timesteps for which at which T-RPMD yields reasonable kinetic energy expectation values for this system (Figs. 3e and f), DF-RPMD yields trajectories that remain reasonably accurate. These results indicate that methods based on dimension-free integration schemes hold promise for the efficient calculation of both static and dynamic quantum mechanical properties.

VIII. SUMMARY

In a previous paper[25], we showed that essentially all schemes for the non-preconditioned equations of motion of PIMD, including the widely used OBABO scheme, lack strong stability due to the use of exact free-ring polymer time evolution in the "A" sub-step, and we proved that this lack of strong stability gives rise to a lack of ergodicity in the thermostatted trajectories. We further showed that ergodicity can be restored by simply replacing the "A" sub step with the Cayley transform.

In the current work, we show that a completely distinct – yet equally important – pathology exists in the "B" sub-step of previously developed non-preconditioned PIMD integrators, due to the outsized effect of the external potential on the dynamics of the high-frequency ring-polymer modes. Specifically, we show that previous integrators yield a numerical stationary distribution for which the overlap with the exact stationary distribution vanishes in the infinite-bead limit. We then showed how to restore this overlap by suitably mollifying the "B" substep, yielding the first non-preconditioned PIMD integrators that are "dimension-free" in the sense that errors in the sampled stationary distribution remain bounded in the infinite-bead limit. In particular, we present the OmCmO integration scheme, for which mollification is applied to internal ring-polymer modes using a criterion that depends only upon the temperature of the simu-

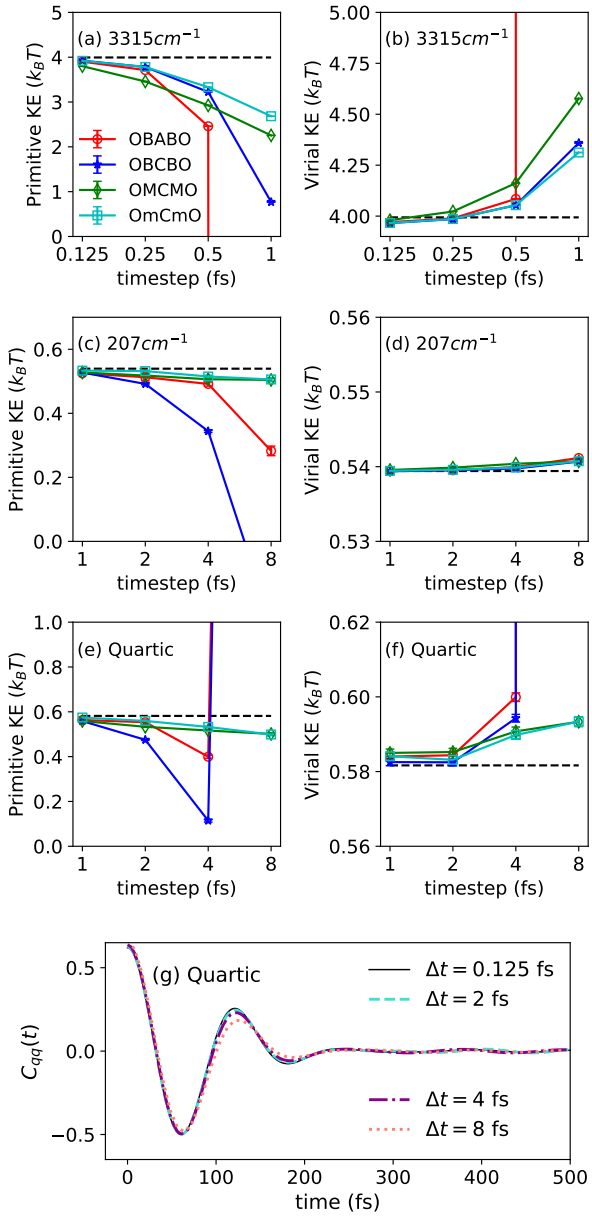

FIG. 3. **Primitive and virial kinetic energy expectation values** as a function of the timestep for the weakly anharmonic potential corresponding to 3315 cm^{-1} at room temperature (a,b), the weakly anharmonic potential corresponding to 207 cm^{-1} at room temperature (c,d), and the quartic potential (e,f). The exact kinetic energy is indicated with a dashed line. Also, the position autorcorrelation function (g) for the quartic oscillator computed using DF-RPMD with various integration timesteps. The DF-RPMD method involves integrating trajectories using the OmCmO scheme and interpreting those trajectories with the usual RPMD model for real-time dynamics. Results are obtained using 64 ring-polymer beads and are plotting using timesteps of $\Delta t = 0.125, 2, 4,$ and 8 fs. It is confirmed that the small-timestep DF-RPMD results are graphically indistinguishable from small-timestep T-RPMD results.

lation and the number of ring-polymer beads employed. This partially mollified scheme is shown to yield excellent accuracy in terms of statistical and dynamical properties in model systems, while allowing for large increases in the integration timestep.

Implementation of the dimension-free (DF) integration schemes presented here involves no significant additional computational cost, no additional parameters, and no increase in algorithmic complexity in comparison to OBABO. We expect methods based on these new integrators (e.g., DF-RPMD) to be widely useful for the non-preconditioned simulation of statistical properties and dynamical properties in future applications.

ACKNOWLEDGMENTS

We thank Andreas Eberle and Ondrej Marsalek for helpful discussions. N. B.-R. acknowledges support from the National Science Foundation under Award No. DMS-1816378 and the Alexander von Humboldt foundation. R. K. and T. F. M. acknowledge support from the Department of Energy under Award No. DE-FOA-0001912 and the Office of Naval Research under Award No. N00014-10-1-0884.

[1] M. Parrinello and A. Rahman, J. Chem. Phys. **80**, 860 (1984).
[2] G. J. Martyna, A. Hughes, and M. E. Tuckerman, J. Chem. Phys. **110**, 3275 (1999).
[3] P. Minary, G. J. Martyna, and M. E. Tuckerman, J. Chem. Phys. **118**, 2510 (2003).
[4] A. Beskos, G. Roberts, A. Stuart, and J. Voss, Stoch. Dyn. **8**, 319 (2008).
[5] A. Beskos, F. Pinski, J. Sanz-Serna, and A. Stuart, Stoch. Process. Their Appl. **121**, 2201 (2011).
[6] J. Lu and Z. Zhou, preprint (2018), arXiv:arXiv:1811.10995.
[7] Z. Zhang, X. Liu, Z. Chen, H. Zheng, K. Yan, and J. Liu, J. Chem. Phys. **147**, 034109 (2017).
[8] J. Liu, D. Li, and X. Liu, J. Chem. Phys. **145**, 024103 (2016).
[9] N. Bou-Rabee and J. M. Sanz-Serna, Acta Numer. **27**, 113 (2018).
[10] N. Bou-Rabee and A. Eberle, preprint (2019), arXiv:1909.07962.
[11] M. E. Tuckerman, B. J. Berne, G. J. Martyna, and M. L. Klein, J. Chem. Phys. **99**, 2796 (1993).
[12] I. R. Craig and D. E. Manolopoulos, J. Chem. Phys. **121**, 3368 (2004).
[13] S. Habershon, D. E. Manolopoulos, T. E. Markland, and T. F. Miller III, Ann. Rev. Phys. Chem. **64**, 387 (2013).
[14] R. P. Feynman and A. R. Hibbs, *Quantum mechanics and path integrals* (McGraw-Hill, 1965).
[15] D. Chandler and P. G. Wolynes, J. Chem. Phys. **74**, 4078 (1981).
[16] T. F. Miller III and D. E. Manolopoulos, J. Chem. Phys. **123**, 154504 (2005).
[17] T. F. Miller III and D. E. Manolopoulos, J. Chem. Phys. **122**, 184503 (2005).
[18] M. Ceriotti, M. Parrinello, T. E. Markland, and D. E. Manolopoulos, J. Chem. Phys. **133**, 124104 (2010).
[19] M. Ceriotti, D. E. Manolopoulos, and M. Parrinello, J. Chem. Phys. **134**, 084104 (2011).
[20] M. Rossi, M. Ceriotti, and D. E. Manolopoulos, J. Chem. Phys. **140**, 234116 (2014).

[21] M. Rossi, V. Kapil, and M. Ceriotti, J. Chem. Phys. **148**, 102301 (2018).
[22] B. Leimkuhler and C. Matthews, J. Chem. Phys. **138**, 174102 (2013).
[23] N. Bou-Rabee, Entropy **16**, 138 (2014).
[24] G. Bussi, D. Donadio, and M. Parrinello, J. Chem. Phys **126**, 14101 (2007).
[25] R. Korol, N. Bou-Rabee, and T. F. Miller III, J. Chem. Phys. **151**, 124103 (2019).
[26] T. Matsubara, Prog. Theor. Phys. **14**, 351 (1955).
[27] In the special case when $\Lambda = 0$, the given condition for OBCBO corrects a sign error in Eq. 37 of Ref.[25].
[28] D. Li, X. Han, Y. Chai, C. Wang, Z. Zhang, Z. Chen, J. Liu, and J. Shao, J. Chem. Phys. **147**, 184104 (2017).
[29] S. Kakutani, Ann. Math. **49**, 214 (1948).
[30] V. I. Bogachev, *Gaussian measures*, 62 (American Mathematical Soc., 1998).
[31] A. Pérez and M. E. Tuckerman, J. Chem. Phys. **135** (2011), 10.1063/1.3609120.
[32] O. Marsalek, P.-Y. Chen, R. Dupuis, M. Benoit, M. Méheut, Z. Bačić, and M. E. Tuckerman, J. Chem. Theory Comput. **10**, 1440 (2014).
[33] J. A. Barker, J. Chem. Phys. **70**, 2914 (1979).
[34] M. F. Herman, E. J. Bruskin, and B. J. Berne, J. Chem. Phys. **76**, 5150 (1982).
[35] B. García-Archilla, J. M. Sanz-Serna, and R. D. Skeel, SIAM J. Sci. Comput. **20**, 930 (1998).
[36] E. Hairer and C. Lubich, SIAM J. Numer. Anal. **38**, 414 (2000).
[37] J. M. Sanz-Serna, SIAM J. Sci. Comput. **46**, 1040 (2008).
[38] R. I. McLachlan and A. Stern, SIAM J. Sci. Comput. **52**, 1378 (2014).
[39] This inequality comes from using Eq. 32 to write $\sum_{j=1}^{\infty} f(\omega_j \Delta t/2) = \mathrm{I}+\mathrm{II}$ where $\mathrm{I} = 2\sum_{j=1}^{\lfloor \hbar\beta/(\pi\Delta t)\rfloor} f(j\pi\Delta t/(\hbar\beta))$ and $\mathrm{II} = 2\sum_{j=\lceil \hbar\beta/(\pi\Delta t)\rceil}^{\infty} f(j\pi\Delta t/(\hbar\beta))$. Then the first term admits the bound $\mathrm{I} \le 2f(1)\hbar\beta/(\pi\Delta t) < 4\hbar\beta/(\pi\Delta t)$, and for the second term we use $\mathrm{II} \le F(1) + \hbar\beta/(\pi\Delta t)\int_1^{\infty} F(x)dx$ where $F(\mathrm{x}) = 2((1-\mathrm{sinc}^2(\mathrm{x}))/\mathrm{x}^2 + 1/\mathrm{x}^2)^2$ is monotone decreasing on $[1,\infty)$ with $F(1) \le 4$ and $\int_1^{\infty} F(x)dx \le 2$.
[40] This quantification uses: (i) $d_{\mathrm{TV}} \le 2d_{\mathrm{H}}$ where d_{TV} is the total variation distance and d_{H} is the Hellinger distance; and (ii) subadditivity of the squared Hellinger distance, which implies that $d_{\mathrm{H}}^2(\mu,\mu_{\Delta t}) \le \sum_{j=1}^{\infty} d_{\mathrm{H}}^2(\mathcal{N}(0,s_j^2),\mathcal{N}(0,s_{j,\Delta t}^2)) \le \sum_{j=1}^{\infty}(1 - s_j^2/s_{j,\Delta t}^2)^2 \le (3\hbar\beta/(\pi\Delta t)+2)\,\frac{\Delta t^4\Lambda^2}{8m^2}$.
[41] A. L. Gibbs and F. E. Su, Int. Stat. Rev. **70**, 419 (2002), 0209021.